energies

MDPI

Article

Measurement of Soot Volume Fraction and Temperature for Oxygen-Enriched Ethylene Combustion Based on Flame Image Processing

Weijie Yan [1,2,*], Dongmei Chen [2], Zuomei Yang [2], Enyu Yan [2] and Peitao Zhao [2]

1 School of Electrical and Power Engineering, China University of Mining and Technology, No. 1, Daxue Road, Xuzhou 221116, China

2 Key Laboratory of Gas and Fire Control for Coal Mines, China University of Mining and Technology, No. 1, Daxue Road, Xuzhou 221116, China; dongmeichen@cumt.edu.cn (D.C.); yangzuomei@cumt.edu.cn (Z.Y.); yanenyu@cumt.edu.cn (E.Y.); p.zhao@cumt.edu.cn (P.Z.)

* Correspondence: yanweijie@cumt.edu.cn; Tel.: +86-516-8359-2000

Academic Editor: Tariq Al-Shemmeri
Received: 27 March 2017; Accepted: 18 May 2017; Published: 27 May 2017

Abstract: A method for simultaneously visualizing the two-dimensional distributions of temperature and soot volume fraction in an ethylene flame was presented. A single-color charge-coupled device (CCD) camera was used to capture the flame image in the visible spectrum considering the broad-response spectrum of the R and G bands of the camera. The directional emissive power of the R and G bands were calibrated and used for measurement. Slightly increased temperatures and reduced soot concentration were predicted in the central flame without self-absorption effects considered, an iterative algorithm was used for eliminating the effect of self-absorption. Nine different cases were presented in the experiment to demonstrate the effects of fuel mass flow rate and oxygen concentration on temperature and soot concentration in three different atmospheres. For ethylene combustion in pure-air atmosphere, as the fuel mass flow rate increased, the maximum temperature slightly decreased, and the maximum soot volume fraction slightly increased. For oxygen fractions of 30%, 40%, and 50% combustion in O_2/N_2 oxygen-enhanced atmospheres, the maximum flame temperatures were 2276, 2451, and 2678 K, whereas combustion in O_2/CO_2 atmospheres were 1916, 2322, and 2535 K. The maximum soot volume fractions were 4.5, 7.0, and 9.5 ppm in oxygen-enriched O_2/N_2 atmosphere and 13.6, 15.3, and 14.8 ppm in oxygen-enriched O_2/CO_2 atmosphere. Compared with the O_2/CO_2 atmosphere, combustion in the oxygen-enriched O_2/N_2 atmosphere produced higher flame temperature and larger soot volume fraction. Preliminary results indicated that this technique is reliable and can be used for combustion diagnosis.

Keywords: oxy-combustion; soot volume fraction; temperature measurement; flame image processing

1. Introduction

Numerous thermal power plants in China use coal as fuel. When dealing with technologies related to coal combustion, particulate removal and CO_2 reduction have to be considered. A potential technique for CO_2 capture is oxy-combustion of coal. O_2/CO_2 combustion is a process of burning coal in a mixture of oxygen and recycled flue gas, generating a CO_2-concentrated sequestration-ready flue gas [1,2]. Success in the implementation of O_2/CO_2 combustion in coal-fired boilers depends on understanding the differences after the replacement of N_2 with CO_2. The difference in the thermal properties of N_2 and CO_2 renders O_2/CO_2 combustion significantly different from air combustion. Therefore, CO_2 participates in the chemical reaction and affects the combustion characteristics, altering the flame temperature, soot, and NO_x formation [3–6]. Knowledge of the temperatures and soot

concentrations in soot flames can provide valuable information to elucidate the processes involved in soot production.

The optical pyrometer has proven to be a practical measurement technique that can provide the distributions of flame temperatures and soot volume fractions in diffusion flames. Two-dimensional (2-D) distributions of soot volume fraction in hydrocarbon flames can be obtained by light extinction [7–9], and 2-color pyrometry combined with laser-induced incandescence (LII) has been proposed by Snelling et al. [10] for measurements of absolute soot volume fraction. Kotzagianni et al. [11] applied laser-induced breakdown spectroscopy (LIBS) for uniform methane–air mixtures spanning a wide range of compositions and for turbulent non-premixed and premixed flames. Flame image processing techniques based on a digital camera used for pyrometric measurements have been used to measure flame temperature and radiative properties [12–21]. In a previous study [18], a color digital camera was used to capture the flame image in visible spectrum. With consideration of the broad response spectrum of the R, G, and B bands of the camera, the directional radiative intensity of the R and G bands were calibrated and used to reconstruct the 2-D distributions of temperature and soot volume fraction of the flame by solving the radiative transfer equation.

In the present study, the inversion of the 2-D distributions of temperature and soot volume fraction from visible flame images obtained with a digital camera is experimentally investigated considering the effect of self-absorption. Meanwhile, a high-resolution lens was used, the flame images of different flame height were composited together using image processing techniques, and the results of the high-resolution measurement were obtained. A co-flow laminar diffusion flame burner under atmospheric pressure was designed to generate ethylene flames in pure air, O_2/N_2, and O_2/CO_2 oxygen-enhanced atmospheres. First, flame radiation spectrum and color flame images in different combustion conditions were captured and analyzed. Subsequently, the effect of fuel flow rate and oxygen concentration on temperature and soot concentration in the three different atmospheres was discussed.

2. Measurement Principle

The measurement of temperature and soot volume fraction is based on the radiative emission from a soot particle, and the line-of-sight radiative intensity is determined by soot, which emits and absorbs radiation:

$$I_\lambda = \int_0^{l_f} \kappa_\lambda(l) I_{b,\lambda}(l) \exp[-\int_l^{l_f} \kappa_\lambda(l')dl']dl \quad (1)$$

where $I_{b,\lambda}(l) = 2\pi hc^2/\lambda^5\left(e^{hc/\lambda kT(l)} - 1\right)$ is the monochromatic blackbody radiative intensity, c is the speed of light, h is Planck's constant, k is the Boltzmann constant. κ_λ is the absorption coefficient (m^{-1}). $\kappa_\lambda(l)I_{b,\lambda}(l)$ is defined as the spectral emission source term, and $\exp[-\int_l^{l_f} \kappa_\lambda(l')dl']$ is the self-absorption term. A color CCD camera is used to obtain flame images in visible spectrum. The R, G, and B data of the flame images represent the relative radiation intensities of the flame. A blackbody furnace is used to calibrate the relationship between the absolute radiation intensity and the raw R, G, and B data of the image obtained by the camera [18], which will be described in a later section. With consideration of the spectral response of the camera, the absolute radiation intensity obtained by the camera from the flame can be expressed as follows:

$$E_i = \int_{\lambda_1}^{\lambda_2} \eta_{i,\lambda} I_\lambda d\lambda = \int_{\lambda_1}^{\lambda_2} \eta_{i,\lambda} \int_0^{l_f} \kappa_\lambda(l) I_{b,\lambda}(l) \exp[-\int_l^{l_f} \kappa_\lambda(l')dl']dld\lambda \quad (2)$$

where $i = (R, G, B)$, and $\eta_{i,\lambda}$ is the relative spectral response efficiency of the camera, and the method used to obtain the spectral characterization of the camera is described in a subsequent section.

To determine the local temperatures $T(l)$ and the soot spectral absorption coefficient $\kappa_\lambda(l)$, Equation (2) is rewritten as:

$$\begin{aligned} E_i &= \int_0^{l_f}\int_{\lambda_1}^{\lambda_2}\eta_{i,\lambda}\kappa_\lambda(l)I_{b,\lambda}(l)\exp[-\int_l^{l_f}\kappa_\lambda(l')dl']d\lambda dl \\ &= \int_0^{l_f}H_i(l)\exp[-\int_l^{l_f}\kappa_\lambda(l')dl']dl \end{aligned} \tag{3}$$

where $H_i(l)=\int_{\lambda_1}^{\lambda_2}\eta_{i,\lambda}\kappa_\lambda(l)I_{b,\lambda}(l)d\lambda$ is the emission source term, and $\exp\left[-\int_l^{l_f}\kappa_\lambda(l')dl'\right]$ represents the self-absorption term.

The self-absorption effect is disregarded during the initial calculation; thus, Equation (3) can be written as:

$$\begin{aligned} E_R &= \int_0^{l_f}H_R(l)dl \\ E_G &= \int_0^{l_f}H_G(l)dl \end{aligned} \tag{4}$$

In the current study, Tikhonov regularization similar to that in the literature [15,22,23] is used to reconstruct $H_R(l)$ and $H_G(l)$. After $H_R(l)$ and $H_G(l)$ are obtained, the local flame temperatures and the soot absorption coefficients can be derived from the ratio of $H_R(l)$ to$H_G(l)$, as shown below:

$$\frac{H_R(l)}{H_G(l)}=\frac{\int_{\lambda_1}^{\lambda_2}\eta_{R,\lambda}\cdot\kappa_\lambda(\lambda)\cdot I_{b\lambda}(\lambda,T)d\lambda}{\int_{\lambda_3}^{\lambda_4}\eta_{G,\lambda}\cdot\kappa_\lambda(\lambda)\cdot I_{b\lambda}(\lambda,T)d\lambda}=\frac{\int_{\lambda_1}^{\lambda_2}\eta_{R,\lambda}\cdot\kappa_\lambda(\lambda)\cdot 2\pi hc^2/\lambda^5\left(e^{hc/\lambda kT(l)}-1\right)d\lambda}{\int_{\lambda_3}^{\lambda_4}\eta_{G,\lambda}\cdot\kappa_\lambda(\lambda)\cdot 2\pi hc^2/\lambda^5\left(e^{hc/\lambda kT(l)}-1\right)d\lambda} \tag{5}$$

According to the Rayleigh approximation, the soot volume fraction with its spectral absorption coefficient is estimated as follows [24,25]:

$$f_v=\kappa_\lambda\cdot\lambda/(6\pi\cdot E(m)) \tag{6}$$

where $E(m)$ is a function of the real and imaginary parts of the refractive index m, expressed as:

$$E(m)=\mathrm{Im}\left|\frac{m_2-1}{m_2+2}\right|=\frac{6nk}{(n^2-k^2+2)2+4n^2k^2} \tag{7}$$

$E(m)$ is typically regarded as a constant independent of the wavelength [18,24,25] with a magnitude of 0.26 in the visible region.

Considering Equation (6) and $H_i(l)=\int_{\lambda_1}^{\lambda_2}\eta_{i,\lambda}\kappa_\lambda(l)I_{b,\lambda}(l)d\lambda$, the emission source terms $H_R(l)$ and $H_R(l)$ can be rewritten as:

$$\begin{aligned} H_R(l) &= \int_{\lambda_1}^{\lambda_2}\eta_{R,\lambda}\frac{f_v(l)\cdot 6\pi\cdot E(m)}{\lambda}I_{b,\lambda}(l)d\lambda \\ H_G(l) &= \int_{\lambda_3}^{\lambda_4}\eta_{G,\lambda}\frac{f_v(l)\cdot 6\pi\cdot E(m)}{\lambda}I_{b,\lambda}(l)d\lambda \end{aligned} \tag{8}$$

Thus, Equation (5) can be expressed as follows:

$$\frac{H_R(l)}{H_G(l)}=\frac{\int_{\lambda_1}^{\lambda_2}\eta_{R,\lambda}\cdot\frac{E(m)}{\lambda}\cdot 2\pi hc^2/\lambda^5\left(e^{hc/\lambda kT(l)}-1\right)d\lambda}{\int_{\lambda_3}^{\lambda_4}\eta_{G,\lambda}\cdot\frac{E(m)}{\lambda}\cdot 2\pi hc^2/\lambda^5\left(e^{hc/\lambda kT(l)}-1\right)d\lambda} \tag{9}$$

Equation (9) contains only one unknown $T(l)$, which can be solved using the Newton-type iterative algorithm. After the temperatures $T(l)$ are obtained, the soot volume fractions $f_v(l)$ can be calculated from Equation (8), and the absorption coefficient $\kappa_\lambda(l)$ can be expressed using Equation (6).

Notably, $\kappa_\lambda(l)$ and $T(l)$ are intermediate computational results; the self-absorption term $\exp\left[-\int_l^{l_f}\kappa_\lambda(l')dl'\right]$ is disregarded. In the current study, the self-absorption effect is corrected using the method similar to that in Ref. [24] in multi-wavelength emission tomography for flame temperature

and soot volume fraction measurements. The self-absorption term $\exp\left[-\int_l^{l_f} \kappa_\lambda(l')dl'\right]$ can be obtained after $\kappa_\lambda(l)$ is determined, and Equation (3) can be expressed as a matrix equation:

$$\begin{aligned} E_R &= \Delta l \times H_{\text{self}} \times H_R = \Delta l' \times H_R \\ E_G &= \Delta l \times H_{\text{self}} \times H_G = \Delta l' \times H_G \end{aligned} \tag{10}$$

where Δl is the length of the path, H_{self} is the self-absorption term, $\Delta l'$ is the updated length of the path that the self-absorption term considers. The reconstructed emission source terms H_R and H_G can be updated using another instance of Tikhonov regularization, and the updated $T(l)$ and $\kappa_\lambda(l)$ can be recalculated by solving Equations (6), (8), and (9). After several iterations, the absorption coefficient $\kappa_\lambda(l)$ and the temperature $T(l)$ are finally calculated to reach convergence so that the self-absorption effect is considered. The whole solution procedure to simultaneously reconstruct 2-D distributions of temperature and soot volume fraction is shown in Figure 1.

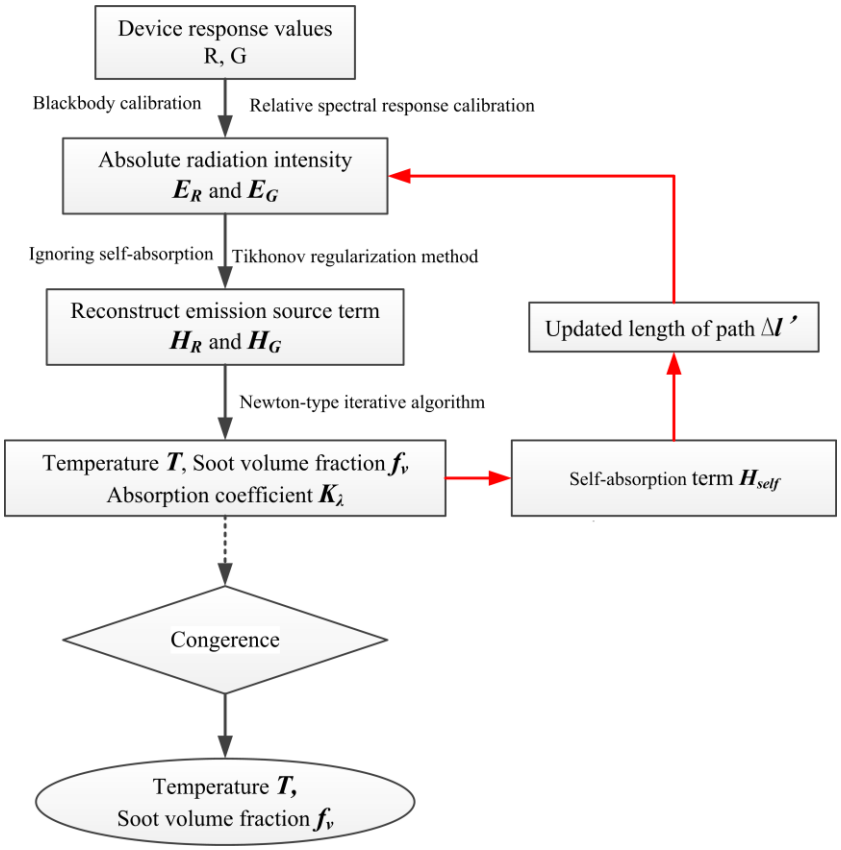

Figure 1. Flow diagram of iterative reconstruction.

3. Measurement Algorithms Validated by Simulation

To validate the performance of the proposed measurement method, some measurement simulations of a fictitious flame with a given temperature and a soot volume fraction were conducted. The temperature of flame and soot volume fraction was measurement by flame emission spectrum taken from Ref. [24]. The relative spectral response of the CCD camera was simply expressed by a Gaussian function during simulation, and by using Equation (2), the absolute radiation intensity of the flames E_R and E_G could be obtained, as shown in Figure 2.

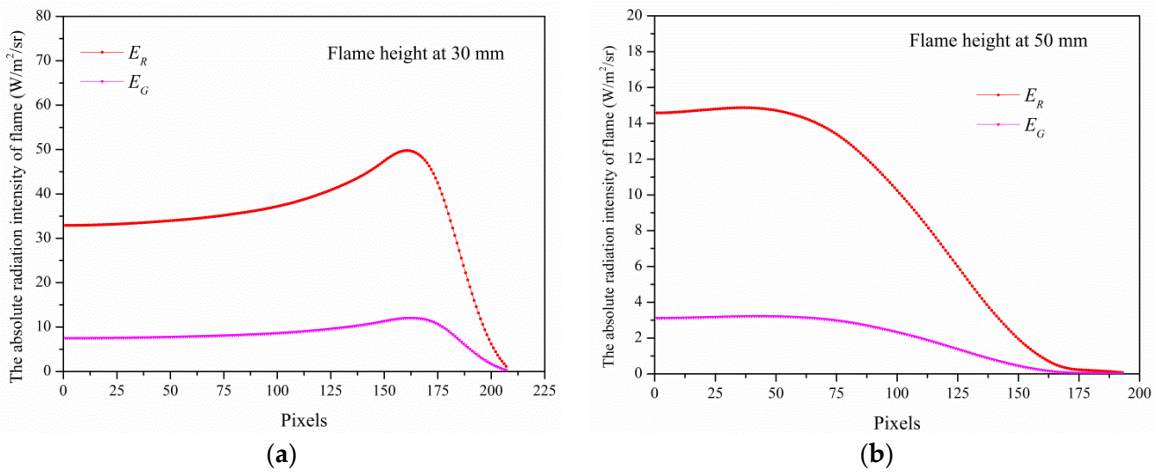

Figure 2. Measurement simulation of the absolute radiation intensity of the flame (**a**) at 30 mm high; and (**b**) at 50 mm high.

The reconstructed emission source terms H_R and H_G could be calculated using E_R and E_G, respectively, on the basis of Tikhonov regularization. The initial values of $T(l)$ and $f_v(l)$ could be obtained in accordance with Equations (6), (8), and (9), and those intermediate results of $T(l)$ and $f_v(l)$ could be used for iterative calculation later. The solution reached convergence as iterations increased, and the convergence value was the final result. In the current study, the convergence was evaluated using $|\Delta f_v|$, and the iterations were considered to be completed if $|\Delta f_v| \leq 0.001$. These changes in the value of the soot volume fraction at a height of 30 mm during iterative calculation are shown in Figure 3.

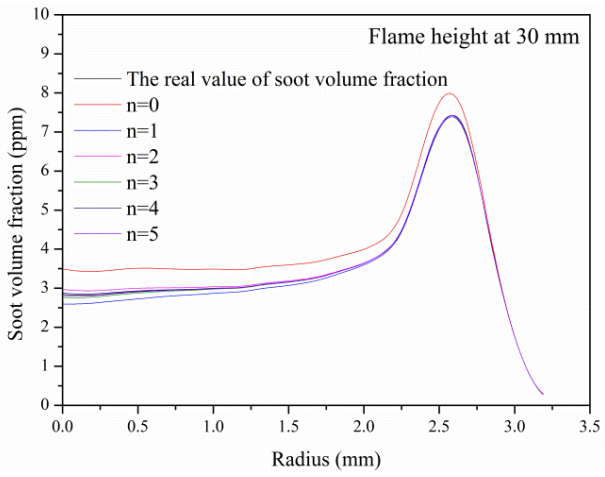

Figure 3. Updated trend value of the soot volume fraction at a height of 30 mm during iterations.

As shown in Figure 3, the calculation value of the soot volume fraction quickly approximates the real value after only one iteration, and the difference between the soot volume fraction calculated using the iterative algorithm and the soot volume fraction in the real-life scenario is not discernible after five iterations. Figure 4 shows the results of the comparison when self-absorption effects are considered and disregarded.

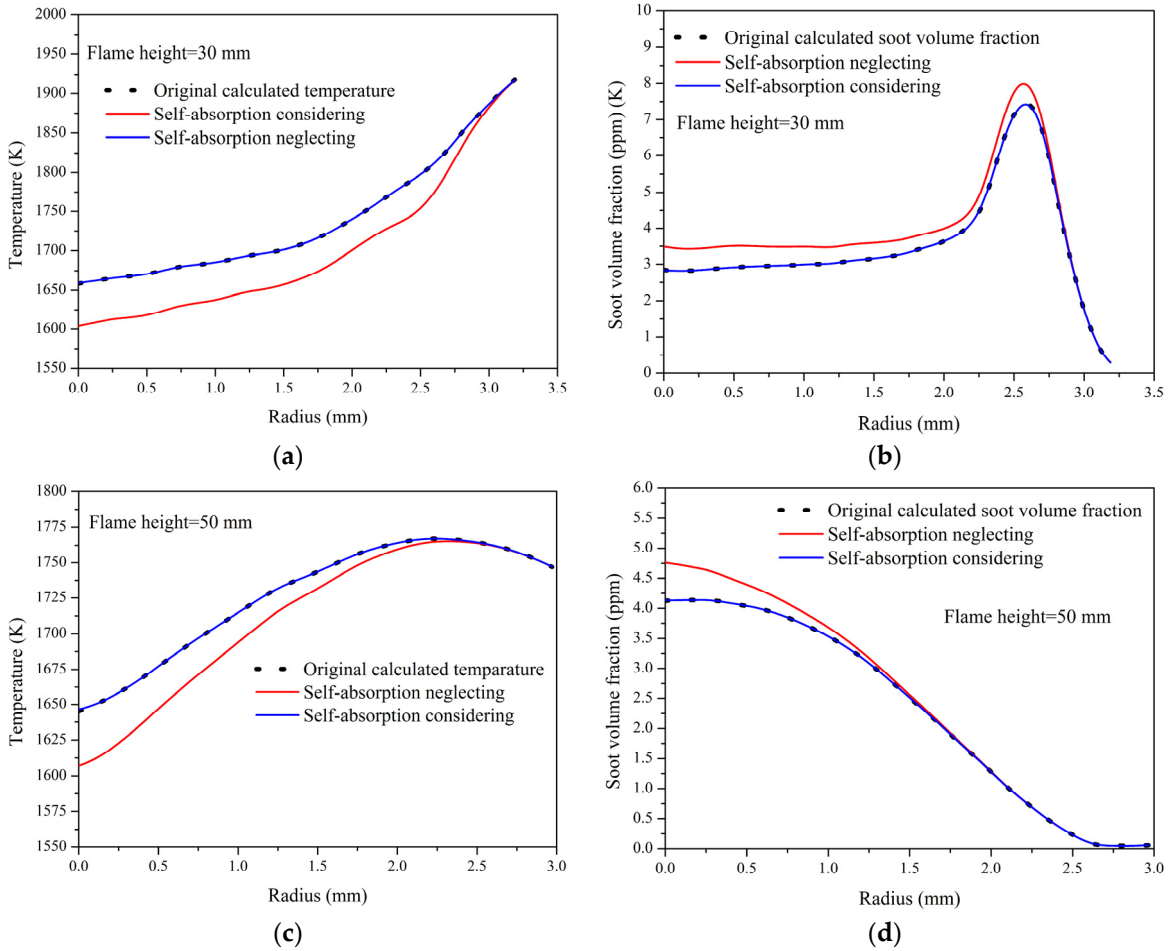

Figure 4. Iteration results with (**a**) temperature at 30 mm; (**b**) soot volume fraction at 30 mm; (**c**) temperature at 50 mm; and (**d**) soot volume fraction at 50 mm.

As shown in Figure 4, both the temperature and the soot volume fraction can be reconstructed accurately when the self-absorption term is considered. The calculation errors of the temperature and the soot volume fraction increase gradually near the center of the flame when the self-absorption term is disregarded. Without the self-absorption term considered, the temperature decreases but the soot volume fraction increases in the central flame. At the flame height of 30 mm, the relative errors in the calculation of the temperature and the soot volume fraction were 3% and 23%, respectively. Thus, the reconstructed results were affected by the self-absorption term and must thus be considered. With the aforementioned results, the performance of the proposed method of flame measurement was proven.

4. Experimental Setup and Calibration

4.1. Experimental Setup

The schematics for burners and experimental equipment is shown in Figure 5. The co-flow burner is similar to the one designed by the National Research Council Canada. The burner consists of a fuel tube with an inner diameter of 10.9 mm, centered in an oxidizer nozzle with an inner diameter of 88 mm and an outer diameter of 100 mm. Electronic mass flow controllers (Type: Sevenstar CS230, Sevenstar Electronics Mass Flow Meter Branch, Beijing, China) with a long-term accuracy of ±1.0% S.P. (≥35% F.S.) governed the flow rates of all gases, and these gases are delivered at room temperature and atmospheric pressure (294 K, 1 atm). Axisymmetric laminar diffusion ethylene flames in pure air, O_2/N_2, and O_2/CO_2 oxygen-enhanced atmospheres were generated by the burner. Figure 6 presents

a photo of the experimental setup. Table 1 summarizes the flow rate of gases in the nine different cases. The adiabatic flame temperatures in Table 1 were calculated using CHEMKIN PRO (ANSYS, Inc., Canonsburg, PA, USA).

The visible flames were captured using a digital camera (Type: Manta G-504, Allied Vision Technologies, Stadtroda, Germany). The camera has a Sony ICX655 sensor (Sony Corporation, Tokyo, Japan) to receive R, G, and B data. The size of the sensor is 2/3 inch with about one million effective pixels (1226 × 1028). Flame images were saved in a 12-bit lossless compressed raw format. To improve the camera resolution, a special telecentric lens (Type: Computar TEC-55, Computar, Tokyo, Japan) with an effective aperture of 33.0 mm was used. The distance between the camera lens and the nozzle center of the burner was 14 cm. In this situation, nearly only the parallel incident light was able to enter the lens, and the barrel distortion of the image was relatively weak. The resolution of the flame image was 64 pixels/mm. To capture the whole flame, the camera was placed on the platform lift, 20 frame flame images were captured at each flame height, and the whole flame image could be obtained by image processing techniques. Figure 7 shows five flame images with different heights and a single composite image.

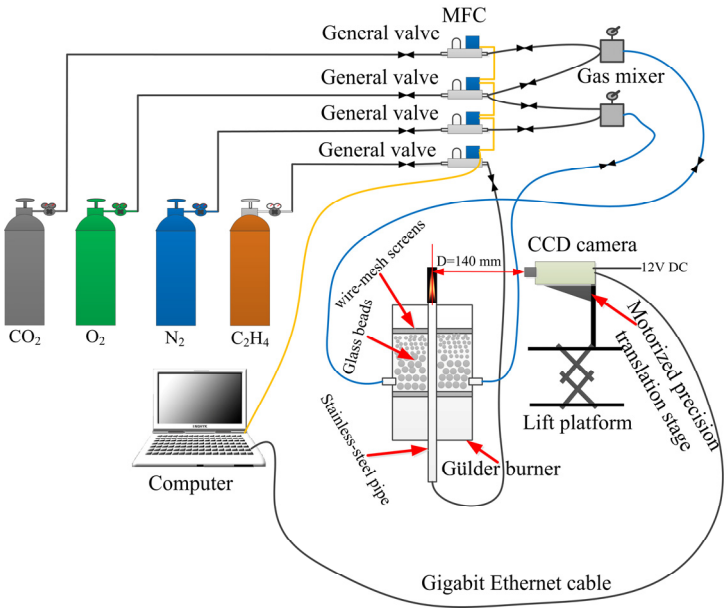

Figure 5. Schematic of the experimental equipment and the burner.

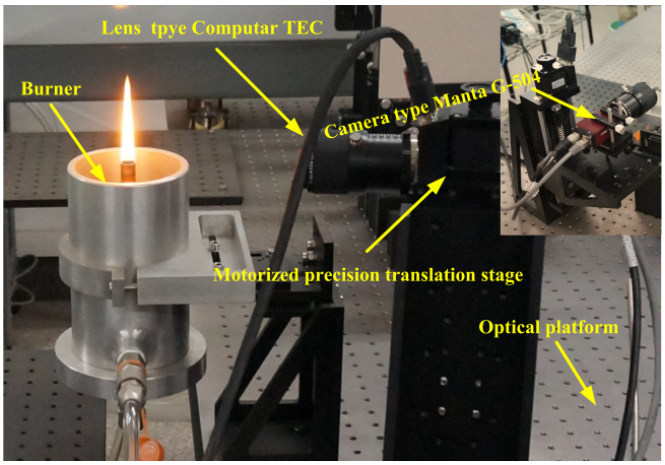

Figure 6. Photo of the digital flame images acquisition system.

Table 1. Experimental conditions.

Case	χ_{O_2}	T_{ad} (K)	$Q_{C_2H_4,1}$ $mL/\min$	$Q_{air,0}$ $L/\min$	$Q_{O_2,0}$ $L/\min$	$Q_{CO_2,0}$ $L/\min$
Case1	21%	2369.0	132	284	0	0
Case2	21%	2369.0	150	284	0	0
Case3	21%	2369.0	194	284	0	0
Case4	30%	2647.6	194	252	32	0
Case5	40%	2818.6	194	216	68	0
Case6	50%	2926.8	194	180	104	0
Case7	30%	2278.0	194	0	85	199
Case8	40%	2517.8	194	0	114	170
Case9	50%	2684.8	194	0	142	142

Note: T_{ad} represents the adiabatic flame temperature, calculated using CHEMKIN PRO.

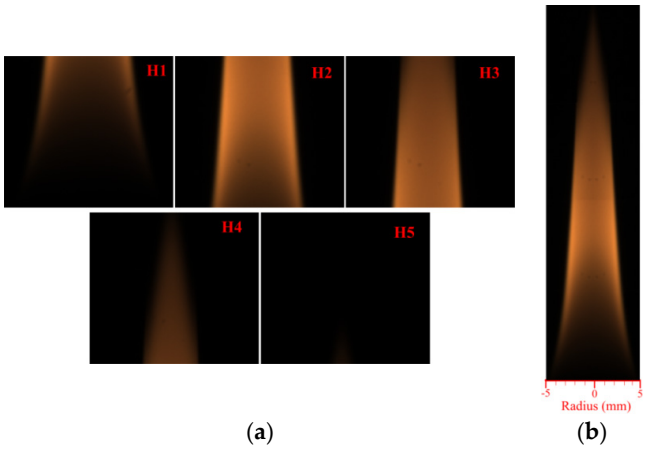

Figure 7. Five different parts of a flame (**a**,**b**) the composite image.

4.2. Calibrations of the Digital Color Camera

Consumer digital cameras are not specifically designed to be used as scientific detectors. To further characterize the cameras, calibration was required. In a previous study on image processing techniques, the R, G, and B data of a pixel in the color digital camera are not proportional to the monochromatic radiative intensities because of the broad spectral response spectra of the R, G, and B bands of the color camera [16–19]. To characterize the relative spectral response of the camera, an experiment similar to Ref. [26] was performed. As shown in Figure 8a, the light source is a 1000 W xenon lamp (Type: OBB Tunable KiloArc, HORIBA Group, Kyoto, Japan), the monochromatic light is obtained with a monochromator, and the light from the monochromator is coupled through a diffuser for the light to be as uniform as possible. The monochromatic light was imaged onto the camera in the visible spectrum of 380–800 nm (negligibly sensitive to non-visible wavelengths for the camera used). The bandwidths of every wavelength are set to 2 nm, although this is not sufficiently narrow for an optical bandwidth. However, this width can sufficiently characterize the relative spectral response of the camera. To obtain sufficiently detailed relative spectral response sensitivity curves, 85 images were taken at each wavelength in steps of 5 nm. Figure 8b shows the typical monochromatic radiation image. Meanwhile, a detector (Trap M), in addition to the camera, whose relative spectral response curves was known, was used to capture monochromatic images controlled by the computer. By using the method described in Ref. [26], the relative spectral response of the camera was obtained. Figure 9 shows the results for the camera (Type: Manta G-504) with lens (Type: Computer TEC-55, Computar, Tokyo, Japan).

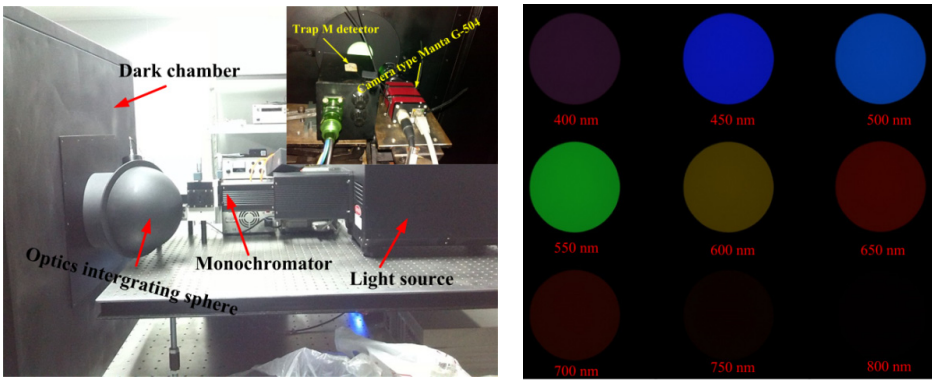

(**a**) (**b**)

Figure 8. (**a**) Camera calibration of relative spectral response setup; and (**b**) Typical monochromatic radiation images.

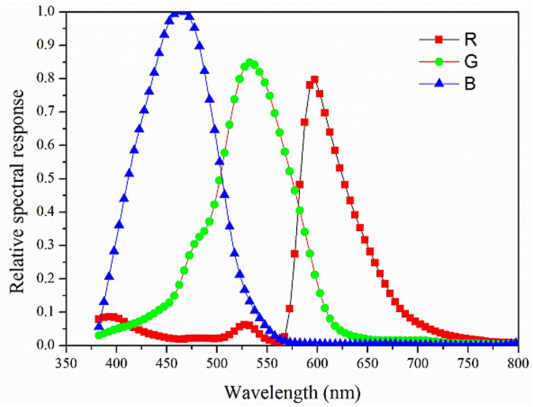

Figure 9. Spectral response curves of the R, G, and B bands of the color digital camera (Type: Manta G-504).

A blackbody furnace (Type: Mikron Model M330) with a temperature range of 300 °C to 1700 °C (temperature uncertainty 0.25% of reading ±1 °C) was used to calibrate the directional emissive powers and the raw data of the R and G bands of the camera, as shown in Figure 10. The variations of $\log(E_R)$ and $\log(E_G)$ with $\log(R/exposure\ time)$ and $\log(G/exposure\ time)$, respectively, are shown in Figure 11.

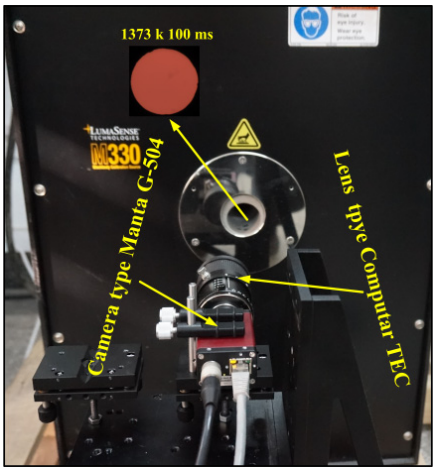

Figure 10. Schematic of the camera blackbody calibration.

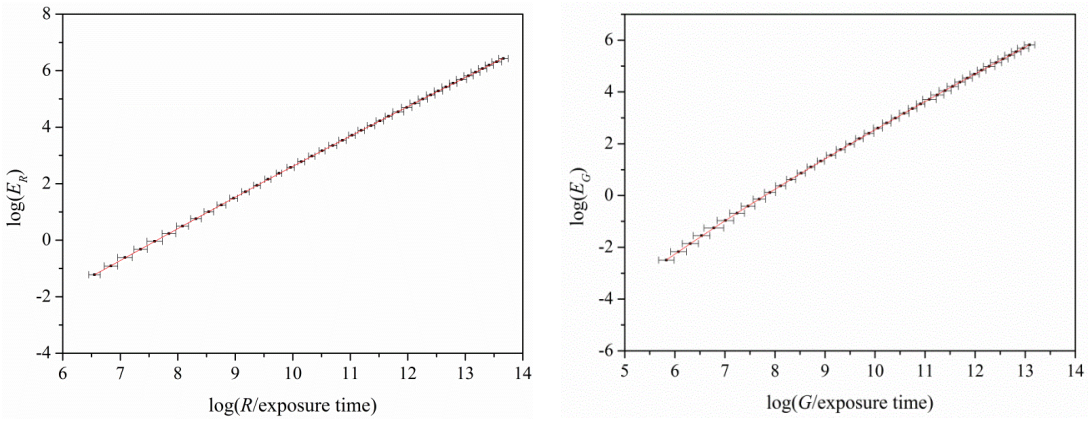

Figure 11. Variations of (**a**) $\log(E_R)$ and (**b**) $\log(E_G)$ with $\log(R/exposure\ time)$ and $\log(G/exposure\ time)$, respectively.

5. Experimental Results and Analysis

The flame images of ethylene combustion in nine different cases are shown in Figure 12. Notably, these images represent the unsaturated flame images, which were used for reconstructing the flame temperature and soot volume fraction. The exposure times were as follows: case1 to case3, 65,000 μs; case4 to case9, 28,000 μs, 12,000 μs, 8500 μs, 60,000 μs, 15,000 μs, 8500 μs, respectively.

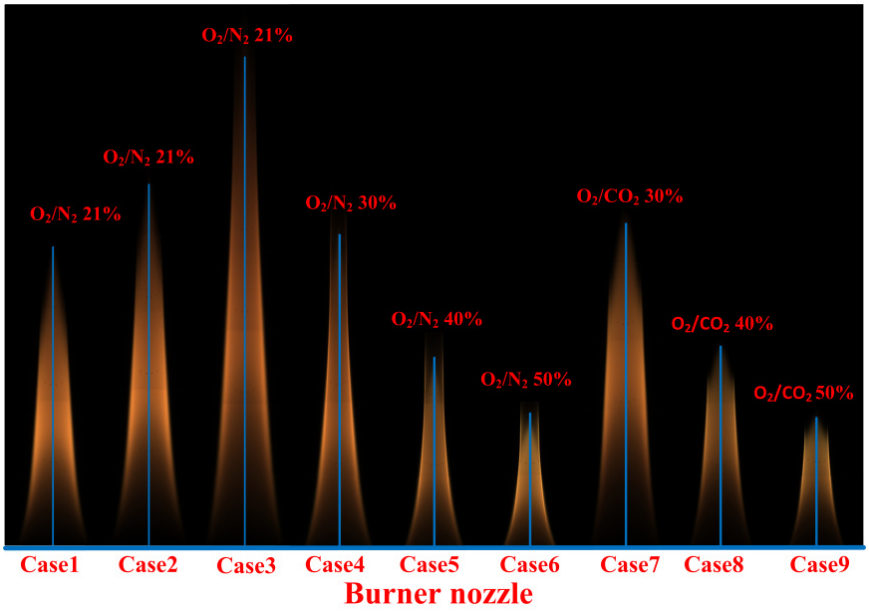

Figure 12. Color images of ethylene flames in pure air atmosphere, O_2/N_2, and O_2/CO_2 oxygen-enhanced atmospheres.

5.1. Pure Air Atmosphere

Case1 to case3 were flame combustion in different fuel flux in pure air atmosphere. The maximum temperatures and soot volume fraction from case1 to case9 are summarized in Table 2. The condition of case3 was similar to that in the literature [24,27]. The C_2H_4 fuel flow rate was set to the smoke point, 194 mL/min (21 °C, 1 atm), and the air co-flow was set to 284 L/min. The maximum soot volume fraction of soot was about 7.8 ppm, and the maximum flame temperature was about 2058 K. The profiles of the temperature and soot volume fraction in the present study were in good agreement

with Ref. [24,27], as shown in Figure 13. The detailed 2-D distribution of temperature and soot volume fraction for case1 is shown in Figure 14. The measurement results for case1 to case3 are shown in Figure 15. Theoretical calculations as those in Table 2 revealed that the adiabatic flame temperature of the three tested cases was equal to 2369.0 K; however, the actual flame temperature was determined by both the chemical reaction heat and the radiant heat. The flame length increased with fuel flow, and soot formation was enhanced because of a lack of oxygen, causing an increase in radiant heat loss. Therefore, the maximum temperature of case1 was higher than that in case2 and case3. Table 2 also shows that the maximum soot volume fractions of case1 and case2 are less than that of case3 because case3 was a smoke point; the incomplete burning is enhanced as fuel flow increases owing to lack of oxygen.

Table 2. Maximum temperatures and soot volume fractions of the nine cases.

Case	χ_{O_2}	L_f(mm)	T_{ad}(K)	$T_{\max}$(K)	f_v(ppm)
Case1	21%	40.1	2369.0	2119	6.8
Case2	21%	51.5	2369.0	2105	7.3
Case3	21%	71.0	2369.0	2057	7.8
Case4	30%	46.2	2647.6	2276	13.6
Case5	40%	29.0	2818.6	2451	15.3
Case6	50%	21.0	2926.8	2678	14.8
Case7	30%	50.9	2278.0	1916	4.5
Case8	40%	30.7	2517.8	2322	7.0
Case9	50%	21.7	2684.8	2535	9.5

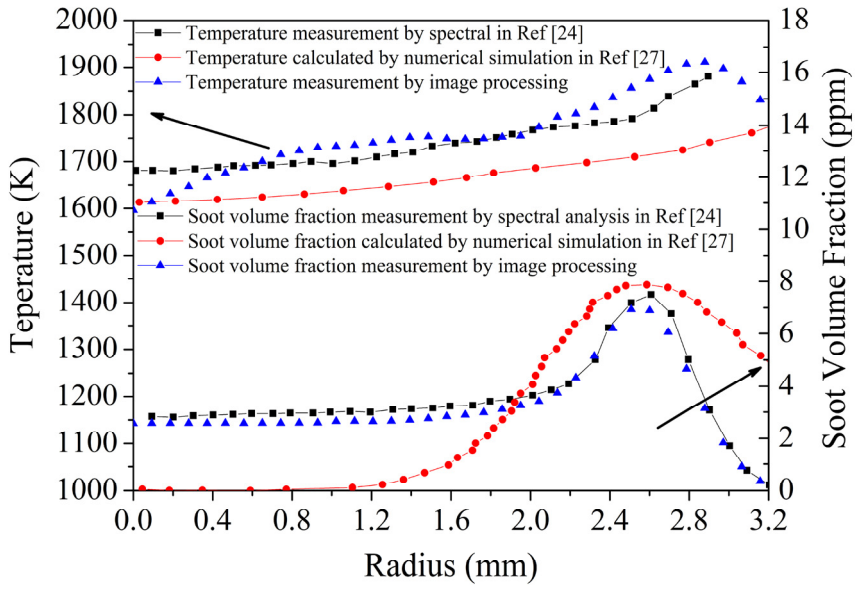

Figure 13. Comparison of temperature and soot volume fraction profiles at flame height z = 30 mm of case 3 with the results in Ref. [24,28].

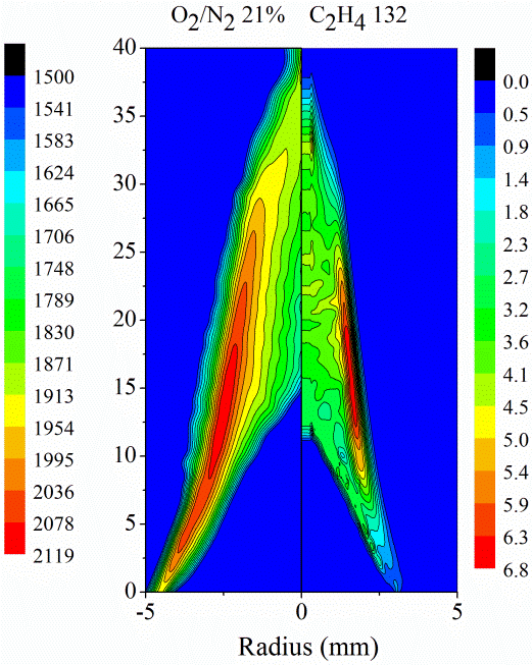

Figure 14. 2-D distributions of temperature T (K) and soot volume fraction (10^{-6}) for case1.

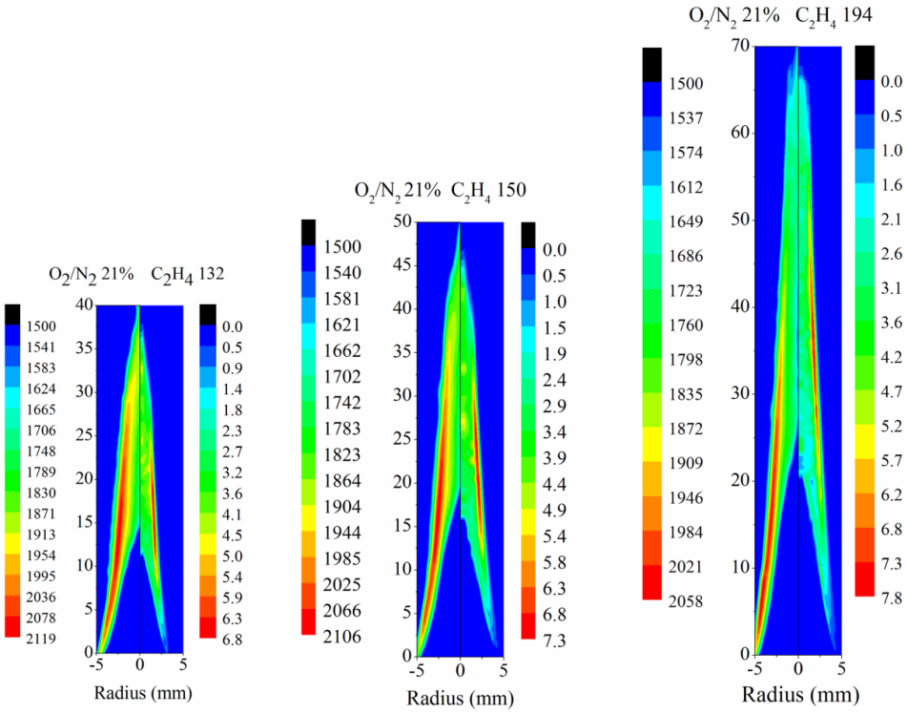

Figure 15. 2-D distributions of temperature T (K) and soot volume fraction (10^{-6}) for C_2H_4 combustion in pure air atmospheres.

5.2. O_2/N_2 Oxygen-Enhanced Atmosphere

As shown in Figure 12, the luminous flame heights are depicted with increasing oxygen concentration in O_2/N_2 oxygen-enhanced atmosphere. This trend agrees with the Roper model. According to Roper's approach [29], a jet diffusion flame ends on the symmetry axis at the point where

oxygen and fuel meet at the stoichiometric ratio, and the point declines along the centerline owing to increases in diffusive oxygen exchange with increasing oxygen concentration.

In Figure 16, the flame temperature contours and soot volume fractions as the oxygen fraction changes from 30% to 50% are plotted. As shown in Figure 16, as the oxygen mole fraction increases, the high-temperature region transitions from the relatively lower wings of the flame to the tip of the flame along the centerline. Meanwhile, the high concentration of the soot region is located in the wings of the flame. The use of the adiabatic flame temperature as the characteristic flame temperature was verified [28,30]. The evidence for the correlation between the adiabatic flame temperatures and the measured maximum temperatures are illustrated in Table 2. As indicated in the table, both the maximum flame temperature and the adiabatic flame temperature increase with increasing oxygen.

Table 2 also suggests that the maximum soot volume fraction initially increases and then decreases with increasing oxygen, and the maximum soot volume fractions are 13.6, 15.3, and 14.8 ppm. This occurrence was attributed to the competition between early nucleation, surface growth, and oxidation [31,32]. The increase in oxygen concentration leads to an increase in peak flame temperature. Such an increase promotes the pyrolysis of the fuel, resulting in the production of hydrocarbon radicals and H atoms, which enhance soot formation. Increased oxygen concentrations also increase the flame temperature, and soot surface growth rates are increased. However, the increased presence of oxygen promotes oxidative mechanisms because of the attack of soot particles by OH and O radicals, tending to diminish soot concentrations.

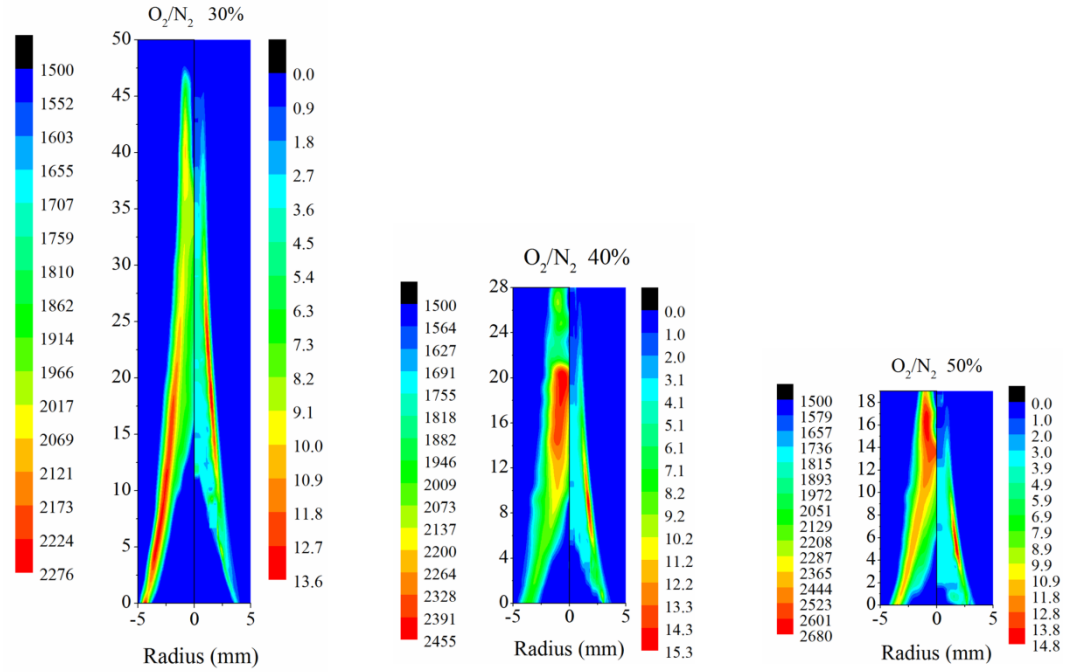

Figure 16. 2-D distributions of temperature T (K) and soot volume fraction (10^{-6}) for C_2H_4 combustion in O_2/N_2 oxygen-enhanced atmospheres.

5.3. O_2/CO_2 Oxygen-Enhanced Atmosphere

Similar to ethylene combustion in O_2/N_2 oxygen-enriched atmosphere, the height of the flame decreased, along with increasing oxygen concentration. A comparison of case7 to case9 in Table 2 suggests that partial replacement of N_2 with the same concentration of CO_2 caused a slight reduction in flame height.

Figure 17 present the measured distributions of temperature and soot volume fraction for case7 to case9. Results in Figure 17 indicate that the high-temperature region transitioned from the wings of the flame to the tip of the flame along the centerline. This occurrence was similar to combustion in O_2/N_2

oxygen-enriched atmosphere. However, the maximum soot volume fraction steadily increased as the oxygen fraction increased, compared with the O_2/N_2 oxygen-enriched atmosphere. Table 2 shows that the maximum temperatures are 1916, 2322, and 2535 K for case7, case8, and case9, respectively. The maximum temperatures are 2276, 2451, and 2678 K for case4, case5, and case6. The reason is that the specific heat capacity of CO_2 is larger than that of N_2, which results in a significant decrease in flame temperature.

Compared with combustion in O_2/N_2 oxygen-enriched atmosphere, the maximum soot volume fractions also decreased with the same mole fraction of O_2. Table 2 reveals that the maximum soot volume fractions are 4.5, 7.0, and 9.5 ppm for case7, case8, and case9. Meanwhile, the maximum soot volume fractions are 13.6, 15.3, and 14.8 ppm for case4, case5, and case6. The decrease in peak temperature results from weakened fuel oxidation. The decrease in flame temperature causes a decrease in the fuel pyrolysis, which leads to a further decline in C_2H_2 and H concentrations, which inhibit soot formation [32]. According to [3,33,34] CO_2 addition exerts chemical effects, in addition to thermal effects, on the reduction in soot formation. The chemical mechanism of CO_2 addition might be to promote the concentrations of oxygen atom and hydroxyl in order to increase the oxidation of soot precursors in soot-forming regions. In a real-life scenario, these effects occur simultaneously and are intimately coupled. Numerical simulation results [3] suggest that the presence of CO_2 in the combustion environment can directly influence the chemical reduction of soot and PAH production tendencies. By promoting the main reaction $CO_2 + H \rightarrow CO + OH$, CO_2 enhances the presence of OH radicals in the post-flame zone, which can be responsible for the oxidation of PAH and soot and most of the chemical destruction of their gaseous precursors.

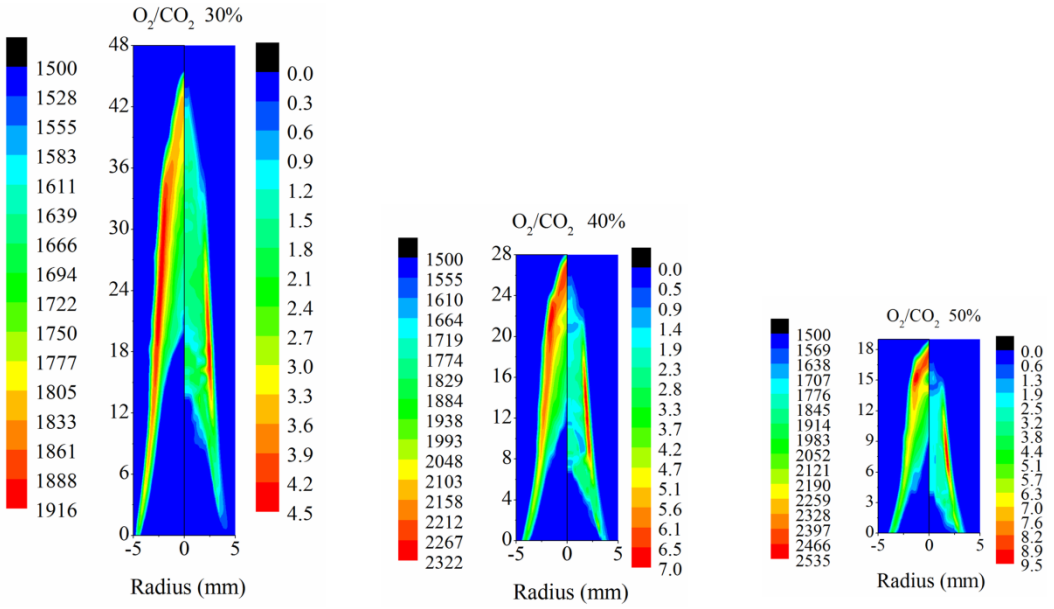

Figure 17. 2-D distributions of temperature T(K) and soot volume fraction (10^{-6}) for C_2H_4 combustion in O_2/CO_2 oxygen-enhanced atmospheres.

6. Conclusions

A method for simultaneously visualizing 2-D distributions of temperature and soot volume fraction in an ethylene soot flame was presented. The radiation visible flame images were used for the measurements. Compared with previous studies, the effect of self-absorption was specifically considered, and the distributions of 2-D temperature and soot volume fraction were obtained. High-resolution images of the flame (1 mm/65 pixels) were obtained using image processing techniques, and those images were used for measurements by solving the radiative transfer equation with iterative reconstruction.

This study evaluated the effects of fuel flow rate and oxygen concentration on the temperature and soot concentration in three different atmospheres. The experiment results indicates that for combustion in a pure air atmosphere, the maximum temperature slightly declined, and the maximum soot volume fraction slightly increased as the fuel mass flow rate increased. For the same oxygen fraction, combustion in O_2/N_2 atmosphere produced both a higher flame temperature and soot volume fraction compared with combustion in O_2/CO_2 oxygen-enriched atmosphere. The results showed that this technique is reliable and can be used for combustion diagnosis.

Acknowledgments: The present study has been supported by the Fundamental Research Funds for the Central Universities, CUMT: 2015QNA14, this work is also a project funded by the Priority Academic Program Development of Jiangsu Higher Education Institutions.

Author Contributions: Weijie Yan conceived and designed the experiments; Weijie Yan, Zuomei Yang, Dongmei Chen and Enyu Yan performed the experiments; Weijie Yan and Peitao Zhao analyzed the data; Weijie Yan wrote the paper.

Conflicts of Interest: The founding sponsors had no role in the design of the study; in the collection, analyses, or interpretation of data; in the writing of the manuscript, and in the decision to publish the results.

References

1. Buhre, B.J.P.; Elliott, L.K.; Sheng, C.D.; Gupta, R.P.; Wall, T.F. Oxy-fuel combustion technology for coal-fired power generation. *Prog. Energy Combust. Sci.* **2005**, *31*, 283–307. [CrossRef]
2. Molina, A.; Shaddix, C.R. Ignition and devolatilization of pulverized bituminous coal particles during oxygen/carbon dioxide coal combustion. *Proc. Combust. Inst.* **2007**, *31*, 1905–1912. [CrossRef]
3. Liu, F.S.; Guo, H.S.; Smallwood, G.J.; Gülder, Ö. The chemical effects of carbon dioxide as an additive in an ethylene diffusion flame: Implications for soot and NO_x formation. *Combust. Flame* **2001**, *125*, 778–787. [CrossRef]
4. Oh, K.C.; Shin, H.D. The effect of oxygen and carbon dioxide concentration on soot formation in non-premixed flames. *Fuel* **2006**, *85*, 615–624. [CrossRef]
5. Watanabe, H.; Yamamoto, J.I.; Okazaki, K. NO_x formation and reduction mechanisms in staged O_2/CO_2 combustion. *Combust. Flame* **2011**, *158*, 1255–1263. [CrossRef]
6. Hecht, E.S.; Shaddix, C.R.M.; Geier, A.; Molina, B.S.H. Effect of CO_2 and steam gasification reactions on the oxy-combustion of pulverized coal char. *Combust. Flame* **2012**, *159*, 3437–3447. [CrossRef]
7. Xu, Y.; Lee, C.F. Forward-illumination light-extinction technique for soot measurement. *Appl. Opt.* **2006**, *45*, 2046–2057. [CrossRef] [PubMed]
8. Thomson, K.A.; Johnson, M.R.; Snelling, D.R.; Smallwood, G.J. Diffuse-light two-dimensional line-of-sight attenuation for soot concentration measurements. *Appl. Opt.* **2008**, *47*, 694–703. [CrossRef] [PubMed]
9. Leschowski, M.; Thomson, K.A.; Snelling, D.R.; Schulz, C.; Smallwood, G.J. Combination of LII and extinction measurements for determination of soot volume fraction and estimation of soot maturity in non-premixed laminar flames. *Appl. Phys. B Lasers Opt.* **2015**, *119*, 685–696. [CrossRef]
10. Snelling, D.R.; Smallwood, G.J.; Liu, F.; Gülder, Ö.L.; Bachalo, W.D. A calibration independent laser-induced incandescence technique for soot measurement by detecting absolute light intensity. *Appl. Opt.* **2005**, *44*, 6773–6785. [CrossRef] [PubMed]
11. Kotzagianni, M.; Yuan, R.; Mastorakos, E.; Couris, S. Laser-induced breakdown spectroscopy measurements of mean mixture fraction in turbulent methane flames with a novel calibration scheme. *Combust. Flame* **2016**, *167*, 72–85. [CrossRef]
12. Vattulainen, J.; Nummela, V.; Hernberg, R.; Kytöla, J. A system for quantitative imaging diagnostics and its application to pyrometric in-cylinder flame-temperature measurements in large diesel engines. *Meas. Sci. Technol.* **2000**, *11*, 103–119. [CrossRef]
13. Lu, G.; Yan, Y.; Riley, G.; Bheemul, H.C. Concurrent measurement of temperature and soot concentration of pulverized coal flames. *IEEE Trans. Instrum. Meas.* **2002**, *51*, 990–995.
14. Wang, F.; Wang, X.J.; Ma, Z.Y.; Yan, J.H.; Chi, Y.; Wei, C.Y.; Ni, M.J.; Cen, K.F. The research on the estimation for the NO_x emissive concentration of the pulverized coal boiler by the flame image processing technique. *Fuel* **2002**, *81*, 2113–2120.

15. Lou, C.; Zhou, H.C.; Yu, P.F.; Jiang, Z.W. Measurements of the flame emissivity and radiative properties of particulate medium in pulverized-coal-fired boiler furnaces by image processing of visible radiation. *Proc. Combust. Inst.* **2007**, *31*, 2771–2778. [CrossRef]
16. Kuhn, P.B.; Ma, B.; Connelly, B.C.; Smooke, M.D.; Long, M.B. Soot and thin-filament pyrometry using a color digital camera. *Proc. Combust. Inst.* **2011**, *33*, 743–750. [CrossRef]
17. Draper, T.S.; Zeltner, D.; Tree, D.R.; Xue, Y.; Tsiava, R. Two-Dimensional flame temperature and emissivity measurements of pulverized oxy-coal flames. *Appl. Energy* **2012**, *95*, 38–44. [CrossRef]
18. Yan, W.J.; Lou, C. Two-Dimensional distributions of temperature and soot volume fraction inversed from visible flame images. *Exp. Therm. Fluid Sci.* **2013**, *50*, 229–233. [CrossRef]
19. Yan, W.J.; Zhou, H.C.; Jiang, Z.W.; Lou, C.; Zhang, X.K.; Chen, D.L. Experiments on measurement of temperature and emissivity of municipal solid waste (msw) combustion by spectral analysis and image processing in visible spectrum. *Energy Fuels* **2013**, *27*, 6754–6762. [CrossRef]
20. Zheng, S.; Zhang, X.Y.; Qi, C.B.; Zhou, H.C. Modeling of heat transfer and pyrolysis reactions in ethylene cracking furnace based on 3-D combustion monitoring. *Int. J. Therm. Sci.* **2015**, *94*, 28–36. [CrossRef]
21. Luo, Z.X.; Xiang, Q.; Cheng, Q.; Lou, C. Changing characteristics of flame images under different oxy-fuel atmospheres in a 3-MW pilot-scale furnace. *IEEE Trans. Instrum. Meas.* **2016**, *10*, 2265–2271. [CrossRef]
22. Åkesson, E.O.; Daun, K.J. Parameter selection methods for axisymmetric flame tomography through Tikhonov regularization. *Appl. Opt.* **2008**, *3*, 407–416. [CrossRef]
23. Revalde1, G.; Zorina, N.; Skudra, A. Line shape measurement and modelling for plasma diagnostics. *J. Phys. Conf. Ser.* **2014**, *548*, 012034. [CrossRef]
24. Snelling, D.R.; Thomson, K.A.; Smallwood, G.J.; Gülder, Ö.; Weckman, E.J.; Fraser, R.A. Spectrally resolved measurement of flame radiation to determine soot temperature and concentration. *AIAA J.* **2002**, *40*, 1789–1795. [CrossRef]
25. Huang, Q.X.; Wang, F.; Liu, D.; Ma, Z.Y.; Yan, J.H.; Chi, Y.; Cen, K.F. Reconstruction of soot temperature and volume fraction profiles of an asymmetric flame using stereoscopic tomography. *Combust. Flame* **2009**, *156*, 565–573. [CrossRef]
26. Fu, T.R.; Cheng, X.F.; Wu, B.; Zhong, M.H.; Shi, C.L.; Liu, T.M. The set-up of a vision pyrometer. *Meas. Sci. Technol.* **2006**, *17*, 659–665. [CrossRef]
27. Guo, H.S.; Liu, F.S.; Smallwood, G.J.; Gülder, Ö.L. Numerical study on the influence of hydrogen addition on soot formation in a laminar ethylene–air diffusion flame. *Combust. Flame* **2006**, *145*, 324–338. [CrossRef]
28. Gomez, A.; Glassman, I. Quantitative comparison of fuel soot formation rates in laminar diffusion flames. *Proc. Combust. Inst.* **1987**, *21*, 1087–1095. [CrossRef]
29. Roper, F.G. The prediction of laminar jet diffusion flame sizes: Part I. theoretical model. *Combust. Flame* **1977**, *29*, 219–226. [CrossRef]
30. Axelbaum, R.L.; Law, C.K. Soot formation and inert addition in diffusion flames. *Proc. Combust. Inst.* **1991**, *23*, 1517–1523. [CrossRef]
31. Choi, M.Y.; Lee, K.O. Effects of turbulence on species mass fractions in methane/air jet flames. *Proc. Combust. Inst.* **1996**, *26*, 1243–1249. [CrossRef]
32. Zhang, J.; Megaridis, C.M. Soot microstructure in steady and flickering laminar methane/air diffusion flames. *Combust. Flame* **1998**, *112*, 473–484.
33. Guo, Z.; Lou, C.; Liu, Z.D.; Zhou, H.C. The impact of combustion characteristics and flame structure on soot formation in oxy-enhanced and oxy-fuel diffusion flames. *Sci. China Technol. Sci.* **2013**, *56*, 1618–1628. [CrossRef]
34. Du, D.X.; Axelbaum, R.L.; Law, C.K. The influence of carbon dioxide and oxygen as additives on soot formation in diffusion flames. *Proc. Combust. Inst.* **1990**, *23*, 1501–1507. [CrossRef]

© 2017 by the authors. Licensee MDPI, Basel, Switzerland. This article is an open access article distributed under the terms and conditions of the Creative Commons Attribution (CC BY) license (http://creativecommons.org/licenses/by/4.0/).